Carbon 130 (2018) 599–606

Contents lists available at ScienceDirect

Carbon

journal homepage: www.elsevier.com/locate/carbon

In situ nitrogen-doped helical mesoporous carbonaceous nanotubes for superior-high lithium anodic performance

Xiang Ao [a, b], Huayan Sun [a], Chundong Wang [b, *], Jiangang Li [a], Yunjun Ruan [b], Baozong Li [a], Qi-Hui Wu [c], Yi Li [a, **], Jianjun Jiang [b], Yonggang Yang [a], Liqiang Mai [d, ***]

[a] Jiangsu Key Laboratory of Advanced Functional Polymer Design and Application, College of Chemistry, Chemical Engineering and Materials Science, Soochow University, Suzhou 215123, PR China
[b] School of Optical and Electronic Information, Huazhong University of Science and Technology, Wuhan 430074, PR China
[c] Department of Materials Chemistry, School of Chemical Engineering and Materials Science, Quanzhou Normal University, Quanzhou 362000, PR China
[d] State Key Laboratory of Advanced Technology for Materials Synthesis and Processing, Wuhan University of Technology, Wuhan 430070, PR China

ARTICLE INFO

Article history:
Received 26 September 2017
Received in revised form
28 December 2017
Accepted 14 January 2018
Available online 18 January 2018

ABSTRACT

Carbon with a theoretical lithium storage capacity of 372 mAh g^{-1} has been widely used in commercial lithium-ion batteries. Increasing the capacity beyond this limit is highly desirable and needed, but challenging. Tailoring the structure and/or introducing heteroatom to carbon lattice may dramatically improve the lithium storage capability. Herein, *in situ* nitrogen-doped helical mesoporous carbonaceous nanotubes with ultra-high specific surface areas of 1170 $m^2 g^{-1}$ are designed. Applied as an anode material for LIBs, the as-prepared sample delivers a superior capacity of 1812 mA h g^{-1} after 150 cycles at a current density of 123 mA g^{-1}, and 1336 mA hg^{-1} after 300 cycles at 372 mA g^{-1}, suggesting that the unique nanoarchitecture provides plentiful lithium ion storage sites and facilitates the electrolyte and electron transport. The lone pairs of electrons of nitrogen atoms would alter the electronic properties of carbon, facilitating electron donation to Li ions. The strategy of rational design and synthesis of carbon nanostructures offer prospects in developing high-performance energy conversion and storage devices/systems.

1. Introduction

Lithium-ion batteries (LIBs), with the merits of long lifespan, environmental benignity, high energy and power density, and low cost, have received considerable attention in the past decades, particularly for the applications in portable electronic devices and electric vehicles [1,2]. Currently, graphite is the main anode material for commercial LIBs [3,4]. However, the low Li theoretical capacity (~370 mAh g^{-1}) and poor rate capability of graphite anode cannot satisfy the requirement of high-energy density and high-power LIBs. To date, much effort has been devoted to searching alternative anode materials with higher specific capacity and rate performance. Non-carbonaceous alloy-type anodes, such as Si, Ge, Sn, Sb and so on, exhibit much higher Li storage capability compared with the commercial graphite anode [5–9]. Unfortunately, these materials experience huge volumetric changes upon Li insertion and extraction, which severely limit their wide applications in LIBs.

Carbonaceous nanomaterials, such as carbon nanotubes [10–12], carbon nanofibers and nanocoils [13,14], porous carbons [15], and graphene [16] have also been extensively explored as anode materials for LIBs. Among them, porous carbons have attracted tremendous attention in LIBs, particularly the nitrogen-doped (N-doping) carbons, owing to their unique structural characteristics of high specific surface area, controllable mesoporous channels, and shortened diffusion length of Li ions, providing a continuous pathway for rapid electron transport and highly accessible surface area for improving rate capability [17,18]. Besides structural benefits, N-doping, which enables strong interaction between carbon and Li ions and facilitates Li insertion, has been suggested to be one of the most effective protocols towards improving Li storage capability [19,20]. Therefore, design and

* Corresponding author.
** Corresponding author.
*** Corresponding author.
E-mail addresses: apcdwang@hust.edu.cn (C. Wang), liyi@suda.edu.cn (Y. Li), mlq518@whut.edu.cn (L. Mai).

https://doi.org/10.1016/j.carbon.2018.01.057
0008-6223/

preparation of novel N-doped carbonaceous electrode materials with ultrahigh specific capacity for Li storage are highly desired.

Basically, the ordered mesoporous carbons can be synthesized via two approaches. One is hard-templating method, in which carbon precursors (such as sucrose, furfuryl alcohol, *in situ* polymerized phenol resin, and aromatic compounds) were grown on the mesoporous silica-based templates, followed by carbonization and removal of the templates, and eventual formation of mesoporous carbons [21–23]. One typical example is the production of mesoporous carbon CMK-3 by using template of mesoporous silica SBA-15 [18,24]. Another approach is the soft-templating method, i.e. supramolecular assemblies of surfactants, together with other carbon sources [25–29]. For example, highly ordered mesoporous resorcinol–formaldehyde (RF) polymers were produced using Pluronic F127 as a template. After calcination under N_2 atmosphere, mesoporous carbons were formed [25,26]. Previously, we have successfully prepared helical carbonaceous nanotubes by utilizing chiral amino acid-derived gelators as the template and helical 3-aminophenol-formaldehyde resin as the carbon sources [30]. Unfortunately, no pores were observed on the walls of the as-prepared helical carbonaceous nanotubes.

Herein, we present a novel strategy to synthesize helical mesoporous carbonaceous nanotubes (HMCNTs), using helical resorcinol-formaldehyde (RF) resin as the carbon source and silica as the pore-maker. First, helical RF resin-silica nanotubes were synthesized in a one-pot reaction by choosing a bola-type cationic gelator as the template, and resorcinol, formaldehyde and tetraethyl orthosilicate (TEOS) serving as the precursors. Subsequently, the carbon-silica nanotubes were formed by carbonization of RF resin-silica nanotubes. Afterward, HMCNTs were obtained after removing the silica temperate with dilute hydrogen fluoride aqueous solution. By virtue of its helical nature and ultra-high specific surface areas (1170 $m^2 g^{-1}$), the as-prepared HMCNTs exhibited superior lithium-ion storage capability. Thus, our study on the newly designed HMCNTs has demonstrated a new concept for nanoarchitecture engineering, opening up new avenues towards exploration of metal-free sustainable energy storage and conversion devices/systems.

2. Experimental

2.1. Materials

Compounds LL-1, whose molecular structure is shown in Fig. 1, was synthesized according to a previous literature [31]. Resorcinol, formaldehyde aqueous solution (37–40 wt%) and anhydrous ethanol were purchased from Aldrich. Concentrated aqueous ammonium hydroxide (25–28 wt%) and tetraethyl orthosilicate (TEOS) were purchased from Sinopharm Chemical Reagent Co., Ltd.

2.2. Characterization of the compounds LL-1

LL-1: ^{1}H NMR (400 MHz, DMSO-d_6, TMS, 20 °C) $\delta = 1.14$ (d, $J = 6.8$ Hz, 6H; CH_3), 1.22–1.50 (m, 48H; alkyl), 1.89–1.94 (m, 4H; CH_2CONH), 2.06–2.10 (m, 4H; $PyCH_2CH_2$), 2.94–3.07 (m, 4H; $CONHCH_2$), 4.20 (t, $J_1 = J_2 = 7.2$ Hz, 2H; NHCHCO), 4.58 (t, $J = 7.6$ Hz, 4H; $PyCH_2$), 7.77 (t, $J = 5.6$ Hz, 2H; $CONHCH_2$), 7.87 (d, $J = 8.0$ Hz, 2H; CONHCH), 8.16 (t, $J = 7.2$ Hz, 4H; 3-PyH), 8.60 (t, $J = 7.6$ Hz, 2H; 4-PyH), 9.08 (d, $J = 5.6$ Hz, 4H; 2-PyH). FT-IR (KBr): 3292 cm^{-1} (ν_{N-H}, amide A), 1638 cm^{-1} ($\nu_{C=O}$, amideI), 1548 cm^{-1} (δ_{N-H}, amideII), 1090 cm^{-1} ($\nu_{Cl=O}$, perchlorate). $C_{50}H_{86}N_6O_{12}Cl_2$ (*M*w: 1034.17). Elemental analysis calcd (%): C, 58.07; H, 8.38; N, 8.13. Found: C, 58.07; H, 7.95; N, 8.34.

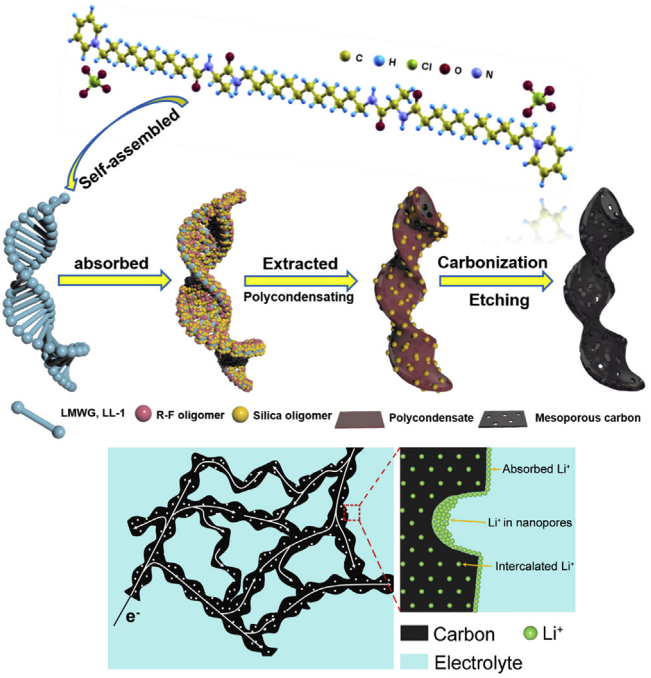

Fig. 1. Molecular structures of the LMWG, LL-1 (top), formation procedure of HMCNT-1 (middle), and schematic representation of Li^+ storage (bottom). (A colour version of this figure can be viewed online.)

2.3. Synthetic procedures

2.3.1. Synthetic of helical resin-silica nanotubes

A typical synthesis route of the resin-silica nanotubes was as follows: LL-1 (200 mg, 0.19 mmol) and resorcinol (180 mg, 1.63 mmol) were dissolved in deionized water (48 mL) and ethanol (2.0 mL) mixed solution at 40 °C under vigorous stirring. Then, concentrated ammonia aqueous solution (0.6 mL, 25–28 wt%), formaldehyde (0.23 mL, 37–40 wt%), and TEOS (0.8 mL, 3.6 mmol) were added into the solution in sequence. The reaction mixture was stirred at 40 °C for 10 h, heated to 80 °C, and then let it stand for 24 h. The as-prepared product was collected by filtration and extracted with ethanol for 48 h to remove the template, and then it was subjected to an oven at 50 °C for 24 h. The obtained sample is brown-reddish powder (denoted as HRSNT-1). For comparison, the as-prepared resin-silica product that collected without removing the template, i.e., resin-silica/template was denoted as HRSNT-2. Helical resin sample (denoted as HRNT) was also prepared according to the same procedure for HRSNT-1, of which the only difference is that no TEOS was added in the reaction mixture.

2.3.2. Synthetic of helical mesoporous carbonaceous nanotubes

The obtained resin-silica sample HRSNT-1 was carbonized at 350 °C for 2.0 h and then 600 °C for 4.0 h with a heating rate of 1.0 °C·min^{-1} in Ar. After cooling to room temperature naturally, carbon-silica sample (denoted as HCSNT-1) was obtained. After that, the carbon-silica sample was immersed in 10 wt% HF aqueous solution at room temperature for 24 h, following which it was washed with deionized water for three times. The as-synthesized sample was then dried in vacuum at 40 °C overnight. The final carbonaceous product was termed as HMCNT-1. Helical mesoporous carbonaceous nanotube HMCNT-2 was synthesized from HRSNT-2 precursor with the same procedures. Moreover, non-porous helical carbonaceous nanotube (donated as HCNT) was also prepared just by carbonization of HRNT under the same conditions.

2.4. Materials characterizations

FE-SEM was performed in a Hitachi 4800 instrument at 300 kV. TEM images were recorded in an FEI TecnaiG220 at 200 kV. WAXRD patterns were collected with an X'Pert-Pro MPD X-ray diffractometer using Cu Kα radiation (1.542 Å). Raman spectra were recorded using a Jobin Yvon Horiba HR 800 LabRAM confocal microprobe Raman system with Ar laser excitation (514.5 nm) and a power of 10 mW. Specific surface area and pore-size distribution were determined by the Brunauer-Emmett-Teller (BET) and Barrett-Joyner-Halon (BJH) methods using N_2 adsorption isotherm measured by a Micromeritics Tristar II 3020 instrument. Thermogravimetric analysis (TGA) was carried out on a Thermal Analysis TG/DTA 6300 instrument with a heating rate of 10 °C min^{-1} and a compressed air flow rate of 200 mL min^{-1}. X-ray photoelectron spectroscopy (XPS) was implemented on an AXIS-ULTRA DLD-600 W spectrometer with Al K_α excitation source.

2.5. Electrochemical measurements

Electrochemical measurements of the samples were evaluated using CR2016 coin-type half-cell assembled in an argon-filled glove box. For preparation of the working electrodes, HMCNT-1 (HMCNT-2 or HCNT), acetylene black (AB) and polyvinylidene fluoride (PVDF) binder (dissolved in N-methylpyrrolidone) were mixed in a mass ratio of 8:1:1. The resultant slurry was then uniformly pasted on a Cu foil current collector and dried overnight under vacuum. Electrochemical cells were assembled with HMCNT-1 (HMCNT-2, HCNT or graphite) electrode as cathode, metallic lithium foil as anode, and Celgard 2325 porous film as separator. The electrolyte used in this work was a solution of 1.0 M LiPF6 dissolved in a mixed solvent of ethylene carbonate (EC), diethyl carbonate (DEC), and dimethyl carbonate (DMC) (1:1:1 by volume). The electrochemical performance of rating and cycling was evaluated in the voltage range of 0.01–3.00 V vs. Li/Li^+ at room temperature. The gravimetric capacity and volumetric capacity were calculated based on the mass loading and volume respectively. Cyclic voltammetry measurements were implemented on an electrochemical workstation (CHI 760E) between 0.01 and 3.0 V vs. Li/Li^+ at a scan rate of 0.01 mV/s. Furthermore, full cells of HMCNT-1 and graphite were also assembled in coin-type cells, in which $LiFePO_4$ was working as the cathode. For preparation of the cathode electrode, a slurry consisting of 92 wt% $LiFePO_4$, 4 wt% AB and 4 wt% PVDF were prepared and pasted on an aluminum foil. As is well known that the capacity of cathode should be ~1.05 times more than that of the anode in full cell; and, the mass loading of active material depends on the measured capacity in the first cycle in a half-cell. Before the test, the batteries need to be charged to 3.45 V at 0.1 C (C = 372 $mAhg^{-1}$), and then constant voltage charging was further carried out until the current density less than 0.02 C toward formation of solid electrolyte interface (SEI) at anode materials. After all of that, the cycling performance of full cells was then evaluated in a voltage range of 2.0 V–3.8 V.

3. Results and discussion

Low molecular weight gelator (LMWGs) derived from amino acids can be self-assembled into various helical nanostructures, which have been widely utilized as templates for preparation of helical silica and hybride silica nanomaterials [31–35]. Herein, we first synthesized a bola-type cationic gelator LL-1, which could self-assembled into left-hand twisted nanoribbons in anhydrous ethanol at a concentration of 20 mg mL^{-1} at 25 °C (see Fig. S1a). The diameters of the gel nanoribbons range from 50 to 100 nm, and the length can be up to several microns. Then, it was used to prepare helical resin-silica nanotubes (HRSNT-1). After polycondensating, further thermosetting and removing of the templates were implemented, HMCNT-1 were obtained. The dynamic formation process of HMCNT-1 is schematic depicted in Fig. 1.

Field-emission scanning electron microscope (FE-SEM) and transmission electron microscope (TEM) images of the resin-silica composite HRSNT-1 are shown in Fig. 2a and d, respectively, which disclose that they are left-handed helical nanotubes. The outer diameters, wall thickness, and helical pitches of the resin-silica nanotubes are 60–100 nm, 15–25 nm, and 400–600 nm, respectively; and the lengths of the nanotubes are several microns. No mesopores can be observed on the HRSNT-1 surface. Upon subjecting HRSNT-1 to high temperature (600 °C for 4.0 h), helical carbon-silica composite HCSNT-1 was obtained, whose SEM and TEM images are demonstrated in Fig. 2b and e. Compared with HRSNT-1, no obvious morphology change was observed in the as-prepared HCSNT-1. Nevertheless, it can be clearly discerned that the outer diameter and wall thickness were all decreased to 50–80 and 10–15 nm, respectively, due to the thermal contraction of RF resin during carbonization processes. Besides, it can be found that the surfaces of HCSNT-1 are rough (Fig. 2e). After etching the silica counterpart in HF aqueous solution, helical mesoporous carbonaceous nanotube HMCNT-1 was obtained as shown in Fig. 2c and f. The thickness of the wall is further reduced to 5–10 nm, and the surface is with densely disordered mesopores as identified in the TEM image (Fig. 2f). For comparison, another two samples, donated as HMCNT-2 (with different N content) and HCNT (without mesopores), were also prepared, the morphologies of which are shown in Figs. S2 and S3. The elemental distribution on selected fork-type tubes in HMCNT-1 was collected by electron energy loss spectroscopy (EELS) mappings, which reveals the uniform distribution of carbon, oxygen and nitrogen over the whole HMCNT-1, informing that the nitrogen and oxygen atoms are efficiently and uniformly incorporated into the carbon matrix. On the other hand, the nanotube structure can be clearly identified by comparing the colour difference between the middle and the edges.

High-resolution TEM (HRTEM) image of HMCNT-1 was recorded (shown in Fig. 3a), disclosing that the as-synthesized HMCNT-1 is composed of randomly oriented graphite-like planes, in other words, it is amorphous. This conclusion is also confirmed by the selected area electron diffraction (SAED) pattern of HMCNT-1, showing a diffuse halo of amorphous carbon in Fig. S4. Again, the tube structure can be well distinguished in Fig. 3a, however, the mesoporous nature cannot be easily identified. To evaluate the porosity and the surface area of the samples of HMCNT-1, HMCNT-2 and HCNT, N_2, adsorption-desorption measurements were implemented. In Fig. 3b, typical H4-type hysteresis loops are observed for HMCNT-1 and HMCNT-2, indicating their slit-like mesopores nature. The sharp capillary-condensation step at P/P_0 between 0.9 and 1.0 in the isotherms indicates the fact that numerous voids exist within the HMCNTs. The BET specific surface areas of HMCNT-1, HMCNT-2 and HCNT are 1170, 904 and 348 $m^2 g^{-1}$, respectively. In the inset of Fig. 3b, the BJH adsorption pore sizes of HMCNT-1 and HMCNT-2 are found to be ~4 nm. Since the pores on the walls of HMCNTs are mainly formed by removal of the fine silica, it manifests that the average size of fine silica aggregates should also be ~4 nm. The XRD pattern and Raman spectrum for HMCNT-1, HMCNT-2 and HCNT are shown in Fig. 3c and d. Two broad diffraction peaks are observed at 23.5° and 43.3° in the XRD patterns of all three samples, corresponding to the (002) and (100) planes of the turbostratic carbon with a low degree of crystallization [36]. However, the (100) peak of HMCNT-1 is the weakest and that of HCNT is the most obvious one, indicating the different crystallinity of these samples. To be specific, the MHCNT-1 exhibits the lowest degree of crystallization, indicating a defect-rich feature

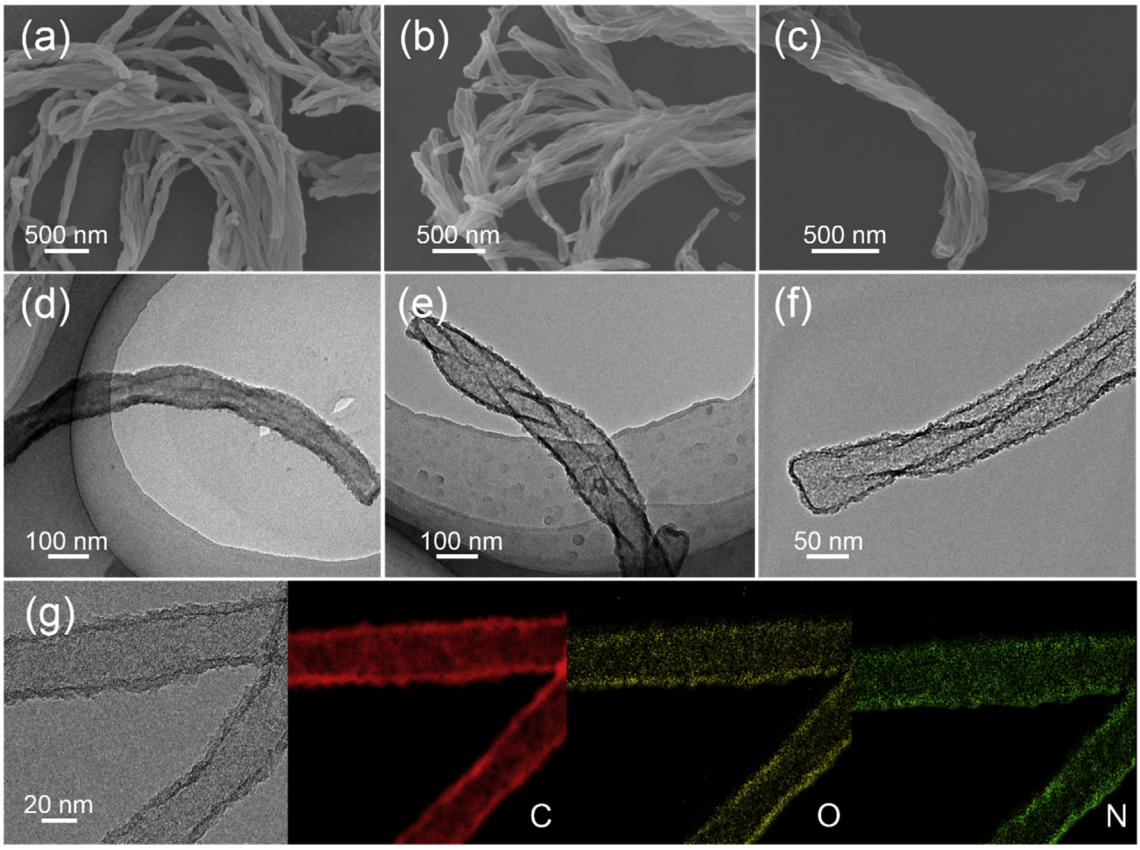

Fig. 2. FE-SEM and TEM images of samples HRSNT-1 (a,d), HCSNT-1 (b,e) and HMCNT-1 (c,f), respectively. (g) EELS elemental mapping images of HMCNT-1. (A colour version of this figure can be viewed online.)

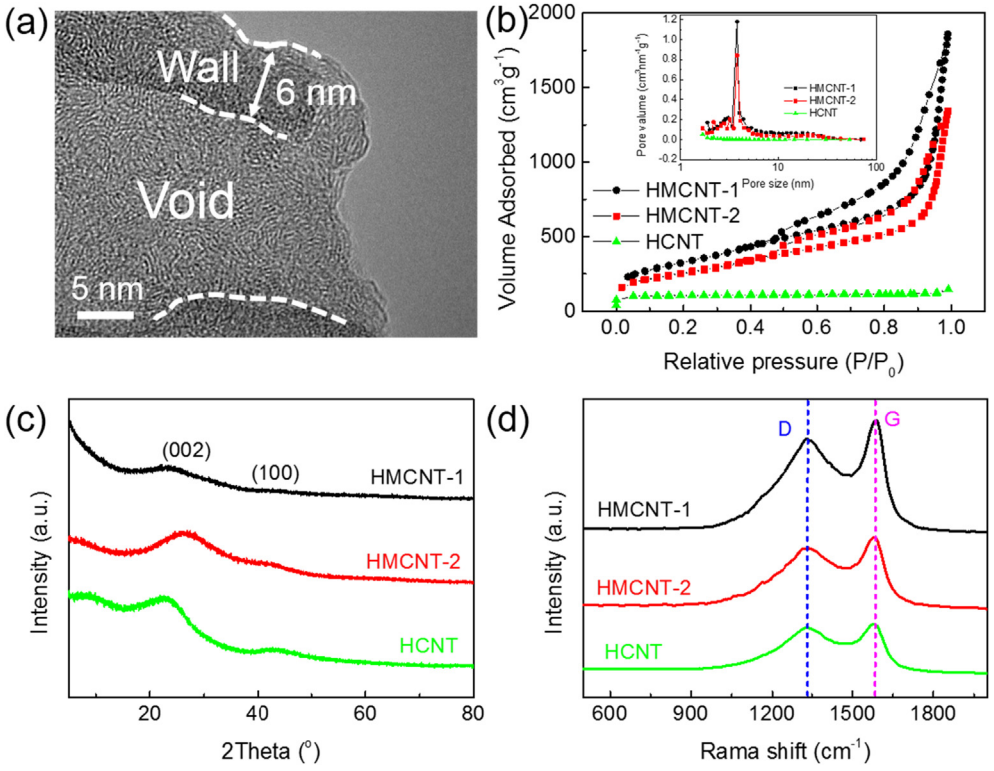

Fig. 3. (a) HRTEM images of HMCNT-1. (b) N_2 adsorption-desorption isotherms of HMCNT-1, HMCNT-2 and HCNT, the inset pore-size distributions of the three samples. (c,d) XRD pattern and Raman spectra of HMCNT-1, HMCNT-2 and HCNT. (A colour version of this figure can be viewed online.)

[37,38]. In the Raman spectrum, two characteristic peaks, i.e. G band (1600 cm^{-1}) and D band (1350 cm^{-1}) are disclosed [39]. I_D/I_G ratio are calculated to be ~2.77, 2.54 and 2.35 for HMCNT-1, HMCNT-2 and HCNT, respectively, corroborating the different crystallinities of carbon deduced from the XRD results [38]. Since the value of I_D/I_G ratio is relevant to the in-plane length (L_a), the mean crystalline size of the sp^2 domains in graphite can be obtained from the following equation, $L_a = C(\lambda)(I_D/I_G)^{-1}$, where $C(\lambda) = 43.5$ Å in the case of $\lambda = 514$ nm [38]. Thus, the values of L_a are calculated to be 1.6, 1.7 and 1.8 nm, respectively, for HMCNT-1, HMCNT-2 and HCNT, indicating that the average crystalline domain size of these samples are very small; in other words, the samples have profuse edge sites, benefiting electron transfer and endowing higher Li storage capacity than the general basal plane.

As revealed in Fig. 2g, nitrogen was *in situ* doped into the as-prepared samples and is uniformly distributed in the carbon matrix. Thus, exploration of the doping concentration and the chemical bonding states of the doped nitrogen atoms is highly preferred. We performed X-ray photoelectron spectroscopy (XPS) measurement on the three samples, and Fig. S5a shows the XPS survey spectra of HMCNT-1, HMCNT-2 and HCNT. The well identified C1s, O1s and N1s peaks indicate the successful incorporation of nitrogen into the carbon lattices. The core level C 1s of HMCNT-1 can be deconvoluted into three evident peaks at about 284.8, 286.3 and 289.0 eV (Fig. 4a-c), attributing to graphitic-like sp^2-C, nitrogen bonded sp^2-C and sp^3-C species, respectively [31,40]. The high resolution XPS spectra of N 1s for HMCNT-1, HMCNT-2 and HCNT are shown in Fig. 4d-f, in which pyridinic N1(~398.4 eV), pyrrolic N2 (~399.9 eV), quaternary N3 (~401.2 eV) and oxidized-N4 groups(~402.8 eV) are observed. From XPS results, the total nitrogen percentages are 1.67, 1.79 and 2.63 at% for HMCNT-1, HMCNT-2 and HCNT, respectively.

Li storage capability of the helical mesoporous carbonaceous nanotubes was evaluated in a coin-type half-cell, with Li metal foils as the counter electrode. To unveil the Li storage mechanism, galvanostatic discharge/charge profiles and cyclic voltammograms (CVs) of the three samples were all collected (see Fig. S6). The cycling performance of HMCNT-1, HMCNT-2, and HCNT were examined at a current density of 0.33 C (1C = 372 mA g^{-1}) over a voltage range of 0.01–3 V versus Li/Li^+. In Fig. 5a, no capacity decay is observed for all the three samples in 150 cycles, exhibiting excellent cyclic stability. In particular, it is noticeable that the capacities of HMCNT-1 and HMCNT-2 remained stable in the first dozens cycles, and then increase gradually afterward, being consistent with the XPS results, that is, the Li contents increased from 48.5 wt% (20 cycles) to 55.8 wt% (100 cycles). This phenomenon is also observed at other tested current densities (see Fig. S7). Actually, such kind gradual increase behavior has been widely observed for anode electrodes [41,42], the reason of which are basically assigned to the formed polymeric gel-like films on the surface of active materials [43]. In our case, the increased capacity should be related to the activating process of the porous carbon materials, leading to improved Li ion accessibility and increased accommodation ability of Li ions [44]. After 150 cycles, the capacities gradually increased to 1812 and 1293 mAh g^{-1} for HMCNT-1 and HMCNT-2, respectively. For comparison, some recent research works on carbon-based and silicon-based anodes are given in Table S1 (Supporting Information), from which it informs us that our product HMCNT-1 nearly delivers the highest specific capacity against the state-of-the-art carbon-based LIBs.

Encouraged by their high Li capacities, the cycling performances of HMCNT-1, HMCNT-2 and HCNT were further evaluated at a high current density of 1C. The cycling behavior in Fig. 5b shows that the capacities of HMCNT-1 and HMCNT-2 keep rising gradually over 300 cycles, reaching 1336 and 905 mAh g^{-1}, respectively. To the best of our knowledge, such an exceedingly high Li storage capacity for carbon nanotubes has been seldom reported, except for the case of the extremely high N-doped carbon (approximately 10 wt%) prepared by Chen and co-workers [45]. For HCNT, stable cycling performance is revealed for over 150 (at 0.33C) and 300 cycles (at 1C), delivering specific capacities of 559 and 366 mAh g^{-1}, respectively. Although the capacities are much lower than those of

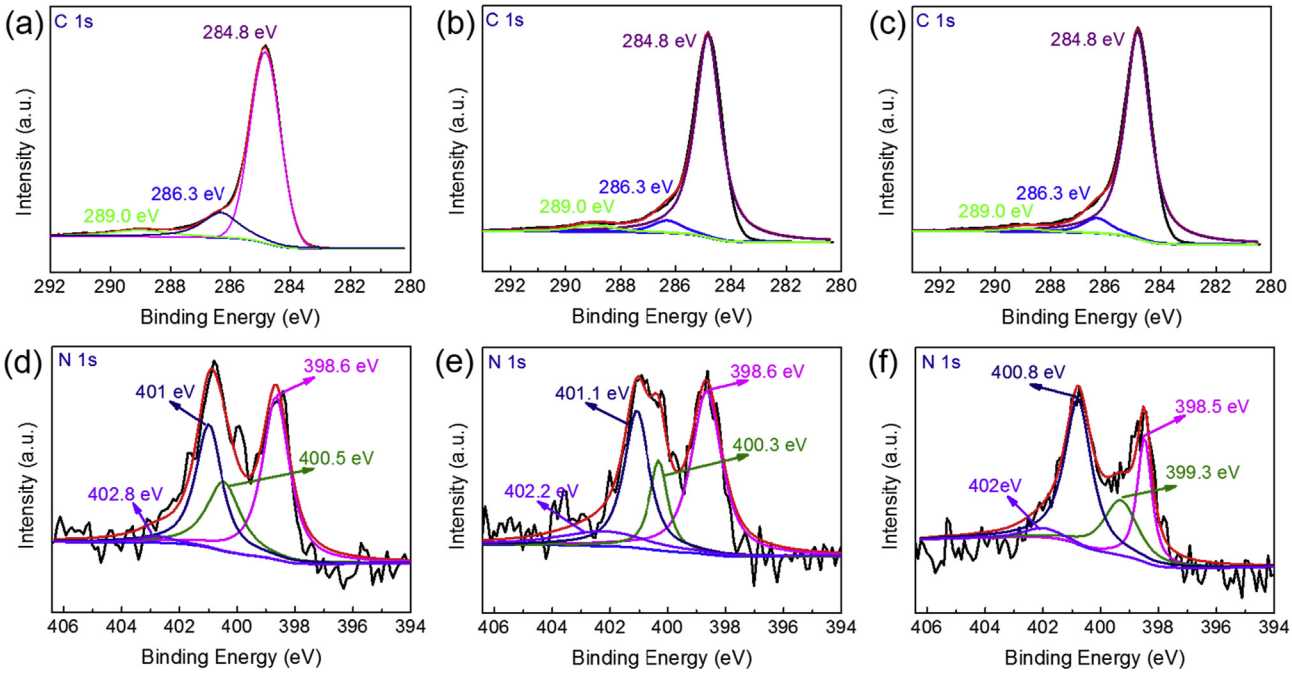

Fig. 4. (a-c) C 1s core level spectra of HMCNT-1, HMCNT-2 and HCNT, (d-f) N 1s core level spectra of HMCNT-1, HMCNT-2 and HCNT. (A colour version of this figure can be viewed online.)

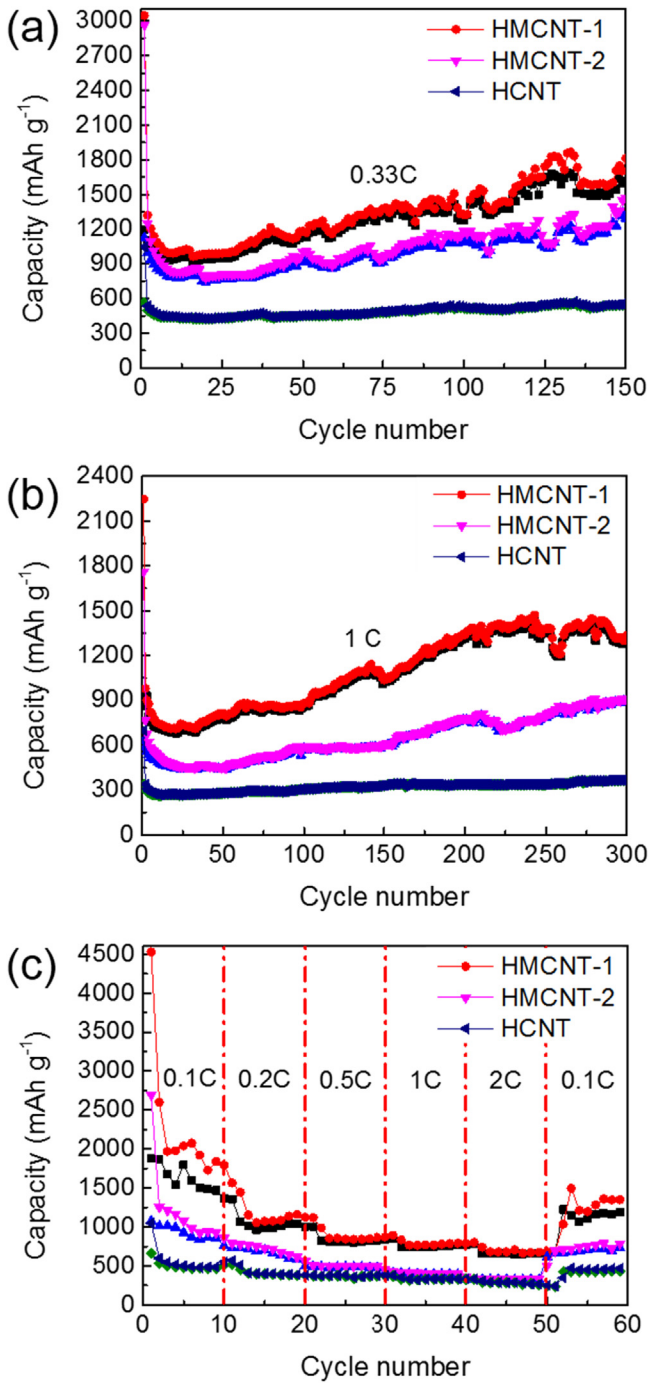

Fig. 5. (a,b) Cycling performance of HMCNT-1, HMCNT-2 and HCNT at current densities of 0.33 C and 1 C. (c) Rate performance at current densities ranging from 0.1 C to 2 C. (A colour version of this figure can be viewed online.)

HMCNT-1 and HMCNT-2, they are close/comparable to the reported value of graphene nanoribbons (GNRS) prepared by unzipping the multi-wall CNT side walls [46]. Besides, volumetric performance of HMCNT-1 was also evaluated, and the similar test was also carried out in graphite electrode to demonstrate the possibility of the practical applications. The volumetric capacity is calculated as gravimetric capacity (mAh g^{-1}) multiply tap density of active material (g cm^{-3}). The mass loadings of HMCNT-1 electrode and graphite electrode are ~0.25 mg and ~0.50 mg respectively, and the thicknesses of active materials that measured by cross-section SEM are ~4.3 μm and ~8.0 μm (see Fig. S8). Additionally, the diameter of electrode is 1.4 cm (geometric area: 1.539 cm^2). Thus, as shown in Fig. S9, the volumetric capacity of HMCNT-1 is calculated to be ~508 mAh cm^{-3}, 74% higher than that of graphite anode. Meanwhile, for the sake of comparison, the electrochemical performance of full cells fabricated with HMCNT-1 and graphite as anode, and $LiFePO_4$ as cathode (termed as HMCNT-1-F and graphite-F) were all evaluated. As shown in Figs. S10a and b, the delivered capacity of HMCNT-1-F is about 300 mAh g^{-1}, much higher than that of graphite. It is noticed that both performance are inferior to that of the commercial full cells, the reason of which could be associated with the quite small contact area of coin cells compared with the pouch-type ones, which results in large resistance. Moreover, compared the capacity delivered in full cells with that obtained in half-cells, we found that the capacity loss of HMCNT-1 (~60%) is less than that of graphite (~90%), the behavior of which could be assigned to the better conductivity of our as-prepared HMCNT-1 (Figs. S10c and d). When the mass loading was increased to ~0.3 mg, the electrode still deliver a high specific capacity, of which the value only has a slight decrease (Fig. S11). By comparison of all the three samples, as well as the previous carbonaceous-based materials [41,45,46], we propose that the extremely large BET surface areas and the mesoporous nature could be the main factors for the exceedingly high specific capacities, as surface, pores and cavities ensure enough spaces for accommodation of Li-atoms [47]. Particularly, the open pores provide easy access to the liquid electrolytes, of which two phase "job-sharing" storage mechanism is involved as suggested by Maier and co-workers [48]. Since carbonization treatment is employed during the preparation process, large amounts of non-equilibrium carbon vacancies should be existing. In this case, lower relaxation energy of the Li filled vacancies (*vs.* the free vacancies) becomes reasonable relating to Li-Li and C-C interactions, allowing more accommodation of Li than the necessary ones toward C-bond saturation [47]. According to previous literature (both theatrical and experimental works), we can determine that the mechanism for the high lithium-storage capacity is not only based on intercalation reaction, but also on the formation of metallic Li-rich phase in the mesoporous carbons [49–51]. Moreover, it is well understood that helical configuration has abundant edges. Li adatoms will diffuse toward the edges, and Li diffusion channels tend to follow along the ribbon axis [52]. Even compared with graphene, lower energy barrier can be achieved toward the edges, resulting in an increase of up to 2 orders of magnitude in the diffusion coefficient. Importantly, from the SEM image of HMCNT-1 electrode after 100 cycles (Fig. S12), we can find that the helical nanotube feature can be still easily identified, informing the robust nature of our prepared helical nanostructure. Besides, we suppose that the *in situ* N-doping could be another possible contributor to the remarkable performance. As the electronegativity and diameter of nitrogen is respectively larger and smaller than that of carbon (i.e. 3.5 *vs* 3.0) [19,45], when nitrogen atoms are incorporated into graphite networks, strong interaction is formed between the N-doped carbon configuration and the Li ions, which is favorable for Li insertion. Previous works reported that with 3.9 atom% N-doping, a reversible capacity of 600–900 mA h g^{-1} could be achieved [19,20]. Thus, we conclude that our remarkable performance should be the synergistic effect of the uniquely designed helical mesoporous architecture and the N-doping.

To further examine the capability of the three samples for high power density LIBs, galvanostatic charge-discharge tests were performed at various current densities, ranging from 0.1 to 2C (Fig. 5c). Outstanding rate capability is demonstrated, particularly for HMCNT-1, showing discharge capacities of 1564, 1124, 892, 803, and 684 mAh g^{-1} at 0.1, 0.2, 0.5, 1, and 2C respectively. When the

current density was shifted back to 0.1C, the average discharge capacity of 1285 mAh g^{-1} was achieved. Even for the worst case here, i.e. sample HCNT, the delivered capacity is still superior to that of RGO-based electrode [53], and comparable to that of tailored graphene nanoribbons [46]. These results indicate that the helical mesoporous carbonaceous nanotubes (HMCNT) could be a promising candidate for a high rate anode material for LIBs.

To gain a further insight into the improved electrochemical performance of mesoporous carbons, EIS measurements of the three samples were collected. Fig. S13 presents the Nyquist plots. As can be seen, each of the electrodes exhibits a depressed semicircle in the high and middle frequency regions followed by a linear tail in the low frequency region. Generally, the semicircle is attributed to summation of the contact, the SEI resistance and the charge-transfer resistance, while the inclined line corresponds to the lithium-diffusion process within carbon electrode. Obviously, the semicircle diameters of HMCNT-1 and HMCNT-2 are similar and rather small with respect to that of HCNT. These observation is as expected and indicates that the helical carbon nanotube with abundant mesopores process a high electrical conductivity and a rapid charge-transfer reaction for lithium ion insertion and extraction.

4. Conclusions

In summary, we demonstrated a novel method for the preparation of helical mesoporous carbonaceous nanotubes, whose density of pores is tunable by using helical resorcinol-formaldehyde resin as the carbon source and silica as the templates. Their applications as anodes for LIBs were presented. The sample HMCNTs with the largest specific surface area (1170 $m^2 g^{-1}$) delivered a specific Li storage capacity of 1812 mA h g^{-1} after 150 cycles at a current density of 123 mA g^{-1}, which is ~5 times more than the theoretical capacity of the commercial graphite. The superior performance of HMCNTs in LIBs was attributed to the rationally designed helical nature nanoarchitecture, *in situ* nitrogen doping, and/or the high specific surface area. Our results highlight the unique potential of designing and tailoring carbon configurations for the preparation of highly porous carbon nanoarchitectures and the applications for batteries.

Acknowledgements

The authors are grateful to the financially supports from the National Natural Science Foundation of China (NSFC Grants No. 51502099, 21574095, 51571096, and 51473106), the Priority Academic Program Development of Jiangsu High Education Institutions (PAPD), the Natural Science Foundation of Hubei Province (No. 2016CFB129), and the Fundamental Research Funds for the Central Universities (No. HUST 2016YXMS211). C.D.W. acknowledges the Hubei "Chu-Tian Young Scholar" program. L.Y. would like to express thanks to Prof. S. -T. Lee, Institute of Functional Nano & Soft Materials (FUNSOM), Soochow University, for his constructive suggestion and kindly help. The authors appreciate the technical support from the Analytical and Testing Center of Huazhong University of Science and Technology.

Appendix A. Supplementary data

Supplementary data related to this article can be found at https://doi.org/10.1016/j.carbon.2018.01.057.

References

[1] J.B. Goodenough, Electrochemical energy storage in a sustainable modern society, Energy Environ. Sci. 7 (1) (2014) 14–18.
[2] J. Ou, Y. Zhang, L. Chen, H. Yuan, D. Xiao, Heteroatom doped porous carbon derived from hair as an anode with high performance for lithium ion batteries, RSC Adv. 4 (109) (2014) 63784–63791.
[3] Y.-P. Wu, E. Rahm, R. Holze, Carbon anode materials for lithium ion batteries, J. Power Sources 114 (2) (2003) 228–236.
[4] C. Wang, D. Li, C.O. Too, G.G. Wallace, Electrochemical properties of graphene paper electrodes used in lithium batteries, Chem. Mater. 21 (13) (2009) 2604–2606.
[5] W.-J. Zhang, A review of the electrochemical performance of alloy anodes for lithium-ion batteries, J. Power Sources 196 (1) (2011) 13–24.
[6] R. Zhang, Y. Du, D. Li, D. Shen, J. Yang, Z. Guo, et al., Highly reversible and large lithium storage in mesoporous Si/C nanocomposite anodes with silicon nanoparticles embedded in a carbon framework, Adv. Mater. 26 (39) (2014) 6749–6755.
[7] B. Luo, B. Wang, X. Li, Y. Jia, M. Liang, L. Zhi, Graphene-Confined Sn nanosheets with enhanced lithium storage capability, Adv. Mater. 24 (26) (2012) 3538–3543.
[8] Y. Zhang, L. Jiang, C. Wang, Preparation of a porous Sn@ C nanocomposite as a high-performance anode material for lithium-ion batteries, Nanoscale 7 (28) (2015) 11940–11944.
[9] X. Ao, J. Jiang, Y. Ruan, Z. Li, Y. Zhang, J. Sun, et al., Honeycomb-inspired design of ultrafine SnO 2@ C nanospheres embedded in carbon film as anode materials for high performance lithium-and sodium-ion battery, J. Power Sources 359 (2017) 340–348.
[10] B.J. Landi, M.J. Ganter, C.D. Cress, R.A. DiLeo, R.P. Raffaelle, Carbon nanotubes for lithium ion batteries, Energy Environ. Sci. 2 (6) (2009) 638–654.
[11] C. De las Casas, W. Li, A review of application of carbon nanotubes for lithium ion battery anode material, J. Power Sources 208 (2012) 74–85.
[12] X.X. Wang, J.N. Wang, H. Chang, Y.F. Zhang, Preparation of short carbon nanotubes and application as an electrode material in Li-Ion batteries, Adv. Funct. Mater. 17 (17) (2007) 3613–3618.
[13] Z.-J. Fan, J. Yan, T. Wei, G.-Q. Ning, L.-J. Zhi, J.-C. Liu, et al., Nanographene-constructed carbon nanofibers grown on graphene sheets by chemical vapor deposition: high-performance anode materials for lithium ion batteries, ACS Nano 5 (4) (2011) 2787–2794.
[14] L. Wang, Z. Liu, Q. Guo, G. Wang, J. Yang, P. Li, et al., Electrochemical properties of carbon nanocoils and hollow graphite fibers as anodes for rechargeable lithium ion batteries, Electrochim. Acta 199 (2016) 204–209.
[15] H. Ru, N. Bai, K. Xiang, W. Zhou, H. Chen, X.S. Zhao, Porous carbons derived from microalgae with enhanced electrochemical performance for lithium-ion batteries, Electrochim. Acta 194 (2016) 10–16.
[16] F. Chen, J. Yang, T. Bai, B. Long, X. Zhou, Facile synthesis of few-layer graphene from biomass waste and its application in lithium ion batteries, J. Electroanal. Chem. 768 (2016) 18–26.
[17] H. Zhou, S. Zhu, M. Hibino, I. Honma, M. Ichihara, Lithium storage in ordered mesoporous carbon (CMK-3) with high reversible specific energy capacity and good cycling performance, Adv. Mater. 15 (24) (2003) 2107–2111.
[18] D. Saikia, T.-H. Wang, C.-J. Chou, J. Fang, L.-D. Tsai, H.-M. Kao, A comparative study of ordered mesoporous carbons with different pore structures as anode materials for lithium-ion batteries, RSC Adv. 5 (53) (2015) 42922–42930.
[19] H. Wang, C. Zhang, Z. Liu, L. Wang, P. Han, H. Xu, et al., Nitrogen-doped graphene nanosheets with excellent lithium storage properties, J. Mater. Chem. 21 (14) (2011) 5430–5434.
[20] X. Wang, Q. Weng, X. Liu, X. Wang, D.-M. Tang, W. Tian, et al., Atomistic origins of high rate capability and capacity of N-doped graphene for lithium storage, Nano Lett. 14 (3) (2014) 1164–1171.
[21] Y. Xia, R. Mokaya, Synthesis of ordered mesoporous carbon and nitrogen-doped carbon materials with graphitic pore walls via a simple chemical vapor deposition method, Adv. Mater. 16 (17) (2004) 1553–1558.
[22] M. Kruk, B. Dufour, E.B. Celer, T. Kowalewski, M. Jaroniec, K. Matyjaszewski, Synthesis of mesoporous carbons using ordered and disordered mesoporous silica templates and polyacrylonitrile as carbon precursor, J. Phys. Chem. B 109 (19) (2005) 9216–9225.
[23] P.F. Fulvio, M. Jaroniec, C. Liang, S. Dai, Polypyrrole-based nitrogen-doped carbon replicas of SBA-15 and SBA-16 containing magnetic nanoparticles, J. Phys. Chem. C 112 (34) (2008) 13126–13133.
[24] H. Qiao, J. Li, J. Fu, D. Kumar, Q. Wei, Y. Cai, et al., Sonochemical synthesis of ordered SnO2/CMK-3 nanocomposites and their lithium storage properties, ACS Appl. Mater. Interfaces 3 (9) (2011) 3704–3708.
[25] J. Xu, X. Zhao, A. Wang, T. Zhang, Synthesis of nitrogen-doped ordered mesoporous carbons for catalytic dehydrochlorination of 1, 2-dichloroethane, Carbon 80 (2014) 610–616.
[26] X. Fang, J. Zang, X. Wang, M.-S. Zheng, N. Zheng, A multiple coating route to hollow carbon spheres with foam-like shells and their applications in supercapacitor and confined catalysis, J. Mater. Chem. A 2 (17) (2014) 6191–6197.
[27] R. Liu, S.M. Mahurin, C. Li, R.R. Unocic, J.C. Idrobo, H. Gao, et al., Dopamine as a carbon source: the controlled synthesis of hollow carbon spheres and yolk-structured carbon nanocomposites, Angew. Chem. Int. Ed. 50 (30) (2011) 6799–6802.
[28] J. Xu, A. Wang, T. Zhang, A two-step synthesis of ordered mesoporous resorcinol–formaldehyde polymer and carbon, Carbon 50 (5) (2012) 1807–1816.
[29] J. Liu, S.Z. Qiao, H. Liu, J. Chen, A. Orpe, D. Zhao, et al., Extension of the Stöber

Method to the preparation of monodisperse resorcinol–formaldehyde resin polymer and carbon spheres, Angew. Chem. Int.l Ed. 50 (26) (2011) 5947–5951.
[30] H. Chen, Y. Li, X. Tang, B. Li, C. Zhang, Y. Yang, Preparation of single-handed helical carbonaceous nanotubes using 3-aminophenol-formaldehyde resin, RSC Adv. 5 (50) (2015) 39946–39951.
[31] C. Zhang, Y. Li, B. Li, Y. Yang, Preparation of single-handed helical carbon/silica and carbonaceous nanotubes by using 4, 4′-biphenylene-bridged polybissilsesquioxane, Chem. Asian J. 8 (11) (2013) 2714–2720.
[32] Y. Yang, M. Suzuki, S. Owa, H. Shirai, K. Hanabusa, Control of mesoporous silica nanostructures and pore-architectures using a thickener and a gelator, J. Am. Chem. Soc. 129 (3) (2007) 581–587.
[33] Y. Fu, B. Li, Z. Huang, Y. Li, Y. Yang, Terminal is important for the helicity of the self-assemblies of dipeptides derived from alanine, Langmuir 29 (20) (2013) 6013–6017.
[34] X. Wu, S. Ji, Y. Li, B. Li, X. Zhu, K. Hanabusa, et al., Helical transfer through nonlocal interactions, J. Am. Chem. Soc. 131 (16) (2009) 5986–5993.
[35] Y. Li, L. Bi, S. Wang, Y. Chen, B. Li, X. Zhu, et al., Preparation of helical mesoporous ethylene–silica nanofibers with lamellar mesopores on the surfaces, Chem. Commun. 46 (15) (2010) 2680–2682.
[36] Z. Li, C. Lu, Z. Xia, Y. Zhou, Z. Luo, X-ray diffraction patterns of graphite and turbostratic carbon, Carbon 45 (8) (2007) 1686–1695.
[37] L. Fu, K. Tang, K. Song, P.A. van Aken, Y. Yu, J. Maier, Nitrogen doped porous carbon fibres as anode materials for sodium ion batteries with excellent rate performance, Nanoscale 6 (3) (2014) 1384–1389.
[38] H.B. Yang, J. Miao, S.F. Hung, J. Chen, H.B. Tao, X. Wang, et al., Identification of catalytic sites for oxygen reduction and oxygen evolution in N-doped graphene materials: Development of highly efficient metal-free bifunctional electrocatalyst, Sci. Adv. 2 (4) (2016), e1501122.
[39] I.Y. Jeon, S. Zhang, L. Zhang, H.J. Choi, J.M. Seo, Z. Xia, et al., Edge-selectively sulfurized graphene nanoplatelets as efficient metal-free electrocatalysts for oxygen reduction reaction: the electron spin effect, Adv. Mater. 25 (42) (2013) 6138–6145.
[40] C. Wang, Y. Zhou, L. He, T.-W. Ng, G. Hong, Q.-H. Wu, et al., In situ nitrogen-doped graphene grown from polydimethylsiloxane by plasma enhanced chemical vapor deposition, Nanoscale 5 (2) (2013) 600–605.
[41] C. Wang, M. Lan, Y. Zhang, H. Bian, M.-F. Yuen, K.K. Ostrikov, et al., Fe 1− x S/C nanocomposites from sugarcane waste-derived microporous carbon for high-performance lithium ion batteries, Green Chem. 18 (10) (2016) 3029–3039.
[42] C. Wang, Y. Li, Y. Ruan, J. Jiang, Q.-H. Wu, ZnFe2O4-nanocrystal-assembled microcages as an anode material for high performance lithium-ion batteries, Mater. Today Energy 3 (2017) 1–8.
[43] Z. Liang, X. Hongyi, Z. Hongwei, Y. Jie, S.B. Hartono, Q. Kun, et al., Cheap and scalable synthesis of a-Fe2O3 multi-shelled hollow spheres as high-performance anode materials for lithium ion batteries, Chem. Commun. 49 (2013) 8695–8697.
[44] Z.-S. Wu, Y. Sun, Y.-Z. Tan, S. Yang, X. Feng, K. Mullen, Three-dimensional graphene-based macro-and mesoporous frameworks for high-performance electrochemical capacitive energy storage, J. Am. Chem. Soc. 134 (48) (2012) 19532–19535.
[45] F. Zheng, Y. Yang, Q. Chen, High lithium anodic performance of highly nitrogen-doped porous carbon prepared from a metal-organic framework, Nat. Commun. 5 (2014) 5261.
[46] C. Wang, Y.-S. Li, J. Jiang, W.-H. Chiang, Controllable tailoring graphene nanoribbons with tunable surface functionalities: an effective strategy toward high-performance lithium-ion batteries, ACS Appl. Mater. Interfaces 7 (31) (2015) 17441–17449.
[47] N.A. Kaskhedikar, J. Maier, Lithium storage in carbon nanostructures, Adv. Mater 21 (25–26) (2009) 2664–2680.
[48] Y.F. Zhukovskii, P. Balaya, E.A. Kotomin, J. Maier, Evidence for interfacial-storage anomaly in nanocomposites for lithium batteries from first-principles simulations, Phys. Rev. Lett. 96 (5) (2006), 058302.
[49] R. Mukherjee, A.V. Thomas, D. Datta, E. Singh, J. Li, O. Eksik, et al., Defect-induced plating of lithium metal within porous graphene networks, Nat. Commun. 5 (2014) 3710.
[50] J.K. Shon, H.S. Lee, G.O. Park, J. Yoon, E. Park, G.S. Park, et al., Discovery of abnormal lithium-storage sites in molybdenum dioxide electrodes, Nat. Commun. 7 (2016) 11049.
[51] D. Datta, J. Li, N. Koratkar, V.B. Shenoy, Enhanced lithiation in defective graphene, Carbon 80 (2014) 305–310.
[52] C. Uthaisar, V. Barone, Edge effects on the characteristics of Li diffusion in graphene, Nano Lett. 10 (8) (2010) 2838–2842.
[53] C. Wang, Q. Zhang, Q.-H. Wu, T.-W. Ng, T. Wong, J. Ren, et al., Facile synthesis of laminate-structured graphene sheet–Fe 3 O 4 nanocomposites with superior high reversible specific capacity and cyclic stability for lithium-ion batteries, RSC Adv. 2 (28) (2012) 10680–10688.